2026 NDIA MICHIGAN CHAPTER
GROUND VEHICLE SYSTEMS ENGINEERING
AND TECHNOLOGY SYMPOSIUM
Autonomy & Robotics Technical Session
AUGUST 11-13, 2026 - NOVI, MICHIGAN

DESIGN AND TESTING OF A LOW-COST INTELLIGENT EMERGENCY STOP SYSTEM FOR AUTONOMOUS GROUND VEHICLES: TRAJECTORY OPTIMIZATION, PATH TRACKING, AND EMBEDDED IMPLEMENTATION

Kyle Thompson[1], David M. Bevly, PhD[1]

[1]Department of Mechanical Engineering, Auburn University, Auburn, AL

ABSTRACT

Advancements in autonomous ground vehicle technology have led to widespread developments in the field. Autonomous ground vehicles require robust emergency stop systems capable of safely managing system failures without human intervention. This paper presents an intelligent emergency stop system that combines minimum-jerk trajectory optimization, linear quadratic regulator path tracking control, and friction-aware velocity planning to perform collision avoidance maneuvers while bringing the vehicle to a controlled stop. The system is designed for implementation on a low-cost single board computer operating as an inline gateway between the main autonomy system and the vehicle CAN bus, providing redundancy against primary system failures. Simulation results, including a 1000-run Monte Carlo analysis, demonstrate robustness to vehicle parameter uncertainty while maintaining tire forces within friction limits. Live testing on a Lincoln MKZ sedan at 30 mph confirmed real-time operation on a $15 Raspberry Pi Zero 2 with lateral tracking errors of less than 15 cm.

Citation: *K. Thompson and D. M. Bevly, "Design and Testing of a Low-Cost Intelligent Emergency Stop System for Autonomous Ground Vehicles: Trajectory Optimization, Path Tracking, and Embedded Implementation," In Proceedings of the Ground Vehicle Systems Engineering and Technology Symposium (GVSETS), NDIA, Novi, MI, Aug. 11–13, 2026.*

1. Introduction

Rapid developments in autonomous technology for unmanned ground vehicles (UGVs) have led to increased potential for the successful fielding of unmanned ground robotic systems across both commercial and military applications. However, these systems still encounter incidents that require either human intervention or a triggered emergency shutdown, especially during the early stages of testing new systems and technologies where failures are most likely to occur [1]. In one large-scale study of autonomous vehicle disengagements, internal system faults accounted for over half of all events (52%), environmental conditions for 11%, and deliberate human takeover for just 30% [1]. For UGVs operating in environments where a human operator cannot be expected to intervene, whether due to communication latency, contested environments, or fully autonomous operation, the vehicle must be capable of safely managing these failures on its own. While many emergency stop (e-stop) scenarios can be addressed by cutting power and applying full brake, a more intelligent solution may be required when the vehicle is operating near obstacles, other vehicles, or in complex terrain [2].

Initial research into vehicle-level emergency stops focused on assisting incapacitated human drivers by using onboard perception and simple planners to guide the vehicle to the roadside [3]. Additional works have further developed methods of planning paths through areas that have been verified as clear of obstacles [4, 5].

In addition to algorithmic work, research has also been done on the hardware required for these systems, including the use of low-cost single board computers for autonomous vehicle control [6]. Keeping the cost of safety hardware low is important to prevent auxiliary systems from significantly increasing the overall cost of the vehicle platform. Architecturally, isolating the safety function on dedicated hardware—decoupled from the primary compute stack—has been shown to improve fault tolerance [7, 5].

This work presents the key contributions from a recent Master's Thesis [8] and provides validation of intelligent emergency stop algorithms designed to run on low-cost embedded hardware for autonomous ground vehicles. A low-cost single board computer was selected that meets the minimum requirements for real-time control and can be installed as a CAN bus gateway ahead of the drive-by-wire interface, as shown in Figure 1. In its passive state the gateway is transparent to normal traffic. Upon an e-stop trigger it assumes control authority and issues its own steering and braking commands. Its physical and computational separation from the autonomy stack ensures continued operation if the primary computer crashes or loses power.

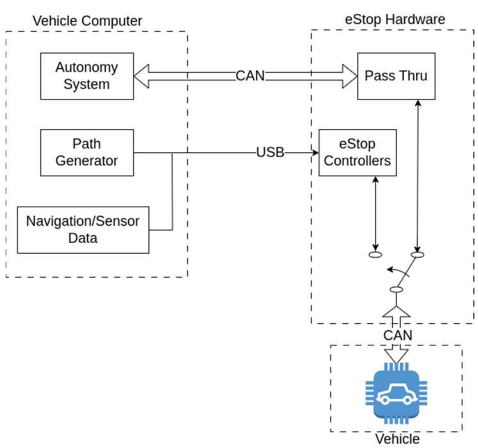

Figure 1: Proposed E-Stop Hardware Configuration

This work assumes that a set of safe waypoints is continuously provided to the e-stop system by an external source, such as a path planner or operator-defined route. The generation of these waypoints is outside the scope of this paper. These waypoints would be capable of capturing the spatial requirements of a simple collision avoidance path like the one shown in Figure 2. A set of lightweight algorithms were developed to be compatible with the constraints of this inexpensive hardware while still providing fast, intelligent, and robust responses to emergency stop triggers, including minimum-jerk trajectory generation, linear quadratic regulator (LQR) path tracking control, and friction-aware velocity planning. These algorithms work to create a system that can produce safe dynamic responses by working to lower dynamic requirements, while maintaining sufficient accuracy in path tracking.

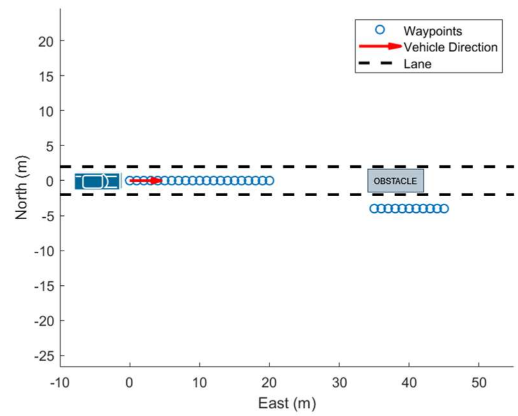

Figure 2: Single Lane Change Collision Avoidance Scenario

2. Modeling

The developed algorithms for ground vehicle autonomy and analysis rely on a set of defined models that represent the behavior of ground vehicle dynamics. This section introduces the models used in this work.

2.1. Lateral Dynamic Bicycle Model

Lateral motion is represented by the well-known dynamic bicycle model, a linearized single-track representation that couples yaw and lateral velocity through a cornering-stiffness tire model [9]. This simplified model defines the lateral motion of the vehicle given steering angle inputs and the vehicle's longitudinal velocity. A visual representation of this model can be seen in the force diagram in Figure 3, and the model parameters are defined in Table 1.

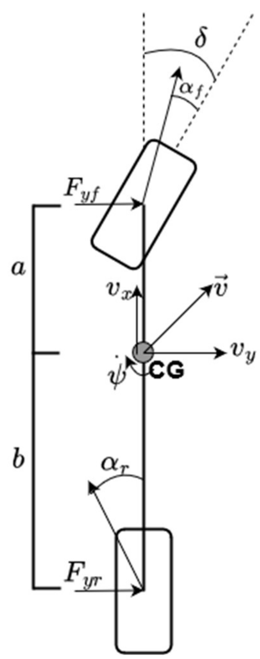

Figure 3: Dynamic Lateral Bicycle Model Force Diagram

Table 1. Bicycle Model Parameters

Symbol	**Description**
$a,\ b$	CG to front/rear axle distance
m	Vehicle mass
I_z	Yaw moment of inertia
$v_x,\ v_y$	Longitudinal, lateral velocity
$\psi,\ \dot{\psi}$	Yaw angle, yaw rate
δ	Steering angle
$C_{\alpha_f},\ C_{\alpha_r}$	Cornering stiffness (front, rear)
$\alpha_f,\ \alpha_r$	Tire slip angle (front, rear)
$F_{yf},\ F_{yr}$	Lateral tire force (front, rear)

Assuming small angles, the tire slip angles at the front and rear axles are:

$$\alpha_f \approx \frac{v_y + a\dot{\psi}}{v_x} - \delta \qquad (1)$$

$$\alpha_r \approx \frac{v_y - b\dot{\psi}}{v_x} \qquad (2)$$

These slip angles produce lateral tire forces through the linear tire model [10], $F_{yf} = -C_{\alpha_f}\alpha_f$ and $F_{yr} = -C_{\alpha_r}\alpha_r$, which drive the lateral dynamics [11]:

$$I_z\ddot{\psi} = aF_{yf} - bF_{yr} \qquad (3)$$

$$m(\dot{v}_y + v_x\dot{\psi}) = F_{yf} + F_{yr} \qquad (4)$$

2.2. Path Tracking Model

For path tracking, the bicycle model is re-expressed in an error frame attached to the nearest point on the reference trajectory [9]. Two error states are defined: the lateral offset e_1, taken as the body-frame cross-track distance to the closest trajectory point, and the heading error e_2, the angle between the vehicle heading and the trajectory tangent at that point. The computation of these reference values from the trajectory spline is detailed in Section 3.3. A visualization of this model is shown in Figure 4.

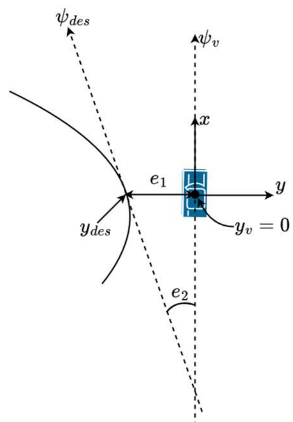

Figure 4: Path Tracking Model Error Visualization

The error states for the path tracking model are defined as:

$$e_1 = -y_{des} \tag{5}$$

$$e_2 = \psi_v - \psi_{des} \tag{6}$$

To recast the bicycle model dynamics in terms of these error states, their second derivatives are needed:

$$\ddot{e}_1 = \dot{v}_y + v_x(\dot{\psi}_v - \dot{\psi}_{des}) \tag{7}$$

$$\ddot{e}_2 = \ddot{\psi}_v - \ddot{\psi}_{des} \tag{8}$$

Substituting Equations (7) and (8) into the force and moment balances of Equations (3) and (4) yields a linear state-space form. The $\ddot{\psi}_{des}$ term represents the rate of change of path curvature, which remains small for the smooth minimum-jerk trajectories used in this work, and thus can be neglected. The resulting system is $\dot{x} = Ax + Bu$ with state $x = [e_1, \dot{e}_1, e_2, \dot{e}_2]^T$ and input $u = [\delta, \dot{\psi}_{des}]^T$. The system matrices are defined as:

$$A = \begin{bmatrix} 0 & 1 & 0 & 0 \\ 0 & a_{22} & a_{23} & a_{24} \\ 0 & 0 & 0 & 1 \\ 0 & a_{42} & a_{43} & a_{44} \end{bmatrix} \tag{9}$$

$$B = \begin{bmatrix} 0 & 0 \\ b_{21} & b_{22} \\ 0 & 0 \\ b_{41} & b_{42} \end{bmatrix} \tag{10}$$

where the non-trivial coefficients are defined in Table 2.

Table 2. State-Space Model Coefficients

Coefficient	Definition
a_{22}	$\frac{-(C_{\alpha_f} + C_{\alpha_r})}{mv_x}$
a_{23}	$\frac{C_{\alpha_f} + C_{\alpha_r}}{m}$
a_{24}	$\frac{-(aC_{\alpha_f} - bC_{\alpha_r})}{mv_x}$
a_{42}	$\frac{-(aC_{\alpha_f} - bC_{\alpha_r})}{I_z v_x}$
a_{43}	$\frac{aC_{\alpha_f} - bC_{\alpha_r}}{I_z}$
a_{44}	$\frac{-(a^2C_{\alpha_f} + b^2C_{\alpha_r})}{I_z v_x}$
b_{21}	$\frac{C_{\alpha_f}}{m}$
b_{22}	$a_{24} - v_x$
b_{41}	$\frac{aC_{\alpha_f}}{I_z}$
b_{42}	a_{44}

3. Algorithms

This section covers the guidance and control algorithms used for the autonomous ground vehicle e-stop system presented in this paper. The techniques used in this section produce a conservative and robust method of safely stopping a vehicle that can be implemented on low cost computing hardware. These algorithms include longitudinal braking control, minimum jerk trajectory optimization, and lateral control.

3.1. Longitudinal Braking Controller

The longitudinal controller targets the smallest constant deceleration that brings the vehicle to rest within a specified distance. A lower deceleration ceiling keeps commanded brake torques well within the range the tires can sustain, reducing the likelihood of wheel lockup or friction-limit violations.

The reference deceleration is derived from basic kinematics. Given the vehicle's current velocity v_0, target velocity v_f, and the distance to the target stop point Δx, the minimum constant acceleration is:

$$a_{cmd} = \frac{v_f^2 - v_0^2}{2\Delta x} \tag{11}$$

where Δx is computed as the sum of distances between waypoints along the e-stop path. For a complete stop, $v_f = 0$.

This reference is converted into a wheel torque command using a feedforward term combined with PID feedback. The feedforward path applies the expected torque for the desired deceleration, while the PID loop corrects any residual velocity error:

$$\tau = R_w m a_{cmd} + k_p e_v + k_d \dot{e}_v + k_i \int e_v \, dt \tag{12}$$

where R_w is the tire radius, m is the vehicle mass, and $e_v = v_{ref} - v_k$ is the error between the expected and measured velocity at each time step.

3.2. Minimum Jerk Trajectory Generation

The e-stop trajectory planner generates smooth stopping paths using minimum jerk optimization. Minimizing jerk produces trajectories with smooth acceleration profiles, which is important for maintaining vehicle stability during an emergency stop where both lateral and longitudinal forces must be managed simultaneously [12].

Following the approach in [13], each spatial dimension of the path is modeled independently as a piecewise 5th-order polynomial in time with $n-1$ segments connecting n waypoints along the safe e-stop route. For a given dimension, each segment carries six coefficients. Stacking all segments yields the decision variable c, which is obtained from the following quadratic program (QP):

$$\min_{c} \; c^T H c \quad \text{s.t. } Ac = b \tag{13}$$

The cost matrix H is block-diagonal, with each block equal to the Hessian of the squared-jerk integral $\nabla^2\left(\int \dddot{x}^2 \, dt\right)$ over one segment. Equality constraints in A enforce waypoint interpolation, C^2 continuity at interior waypoints, and prescribed position, velocity, and acceleration at the trajectory endpoints.

After using Equation (11) to produce the commanded kinematic acceleration, a_{cmd}, the arrival time for each waypoint, t_k, can be found using Equation (14), where v_0 is the initial vehicle velocity and d_k is the Euclidean distance to each waypoint.

$$\frac{1}{2} a_{cmd} t_k^2 + v_0 t_k - d_k = 0 \tag{14}$$

The QP is solved independently for the x and y dimensions using the same segment times, producing two sets of spline coefficients that define the complete two-dimensional stopping trajectory. This formulation is lightweight enough to solve in real time on the candidate low cost embedded hardware.

A comparison of the minimum jerk trajectory against a standard cubic spline interpolation is shown in Figure 5. Although path geometry is comparable between the two methods, the minimum jerk optimization formulation spreads acceleration demands more uniformly along the path, yielding a lower peak value. A cubic spline has no mechanism to account for the vehicle's kinematic state and instead exhibits sharp acceleration spikes at segment transitions. This reduction in peak forces is critical during an emergency stop, where exceeding available tire forces could result in loss of vehicle control.

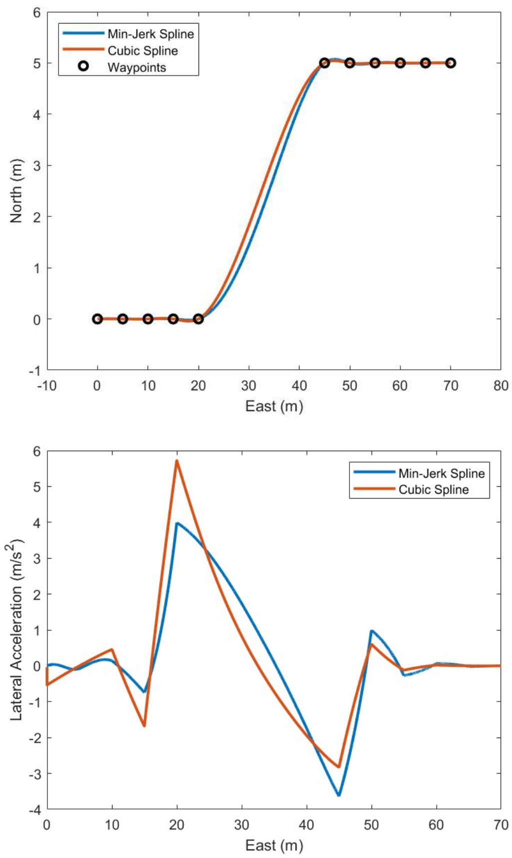

Figure 5: Minimum jerk vs. cubic spline comparison. Top: planned trajectories. Bottom: lateral acceleration requirements.

3.3. Lateral Controller

The lateral controller is a Linear Quadratic Regulator (LQR) operating on the path tracking error model from Section 2.2. Classical pole placement is ill-suited here because the plant matrices change with speed. Selecting a single set of closed-loop eigenvalues leads to erratic gain variation as the vehicle decelerates. An LQR formulation avoids this issue. Constant weight matrices Q and R yield smooth, bounded gains over the entire velocity envelope of a stopping event.

The LQR minimizes the infinite-horizon cost function:

$$J = \frac{1}{2}\int_0^\infty (x^T Q x + u^T R u)\, dt \qquad (15)$$

with Q and R as symmetric positive-definite matrices, weighting the tracking error and the steering effort. The solution produces a state feedback control law $\delta = -Kx + \delta_{ff}$, where K is the optimal gain matrix computed from the algebraic Riccati equation associated with Equation (15) [14].

The reference states for the controller are derived from the minimum jerk trajectory spline, as illustrated in Figure 6. At each time step, the closest point on the spline is found, and the spline derivatives at that point are evaluated to compute the path heading and curvature. The reference heading at that point equals the tangent angle of the spline:

$$\psi_{des} = \tan^{-1}\left(\frac{\dot{x}(t)}{\dot{y}(t)}\right) \qquad (16)$$

The radius of curvature at the closest point is computed from the spline derivatives:

$$R = \frac{\left(\dot{x}(t)^2 + \dot{y}(t)^2\right)^{3/2}}{\dot{x}(t)\ddot{y}(t) - \ddot{x}(t)\dot{y}(t)} \qquad (17)$$

which gives the desired yaw rate as $\dot{\psi}_{des} = v_x/R$. These values are used to compute the error states from Equations (5) and (6) and their derivatives. On curved segments, feedback alone leaves a persistent lateral offset. To eliminate this offset, the steady-state response of the closed-loop system is set to zero lateral error and solved for the required steering input as a function of curvature:

$$\eta = \frac{b}{C_{\alpha_f}} - \frac{a}{C_{\alpha_r}} + \frac{a}{C_{\alpha_r}} k_3 \qquad (18)$$

$$\delta_{ff} = \frac{m v_x^2}{LR}\,\eta + \frac{L}{R} - \frac{b}{R} k_3 \qquad (19)$$

where $L = a + b$ is the wheelbase, k_3 is the yaw error gain from K, and R is the radius of curvature from Equation (17).

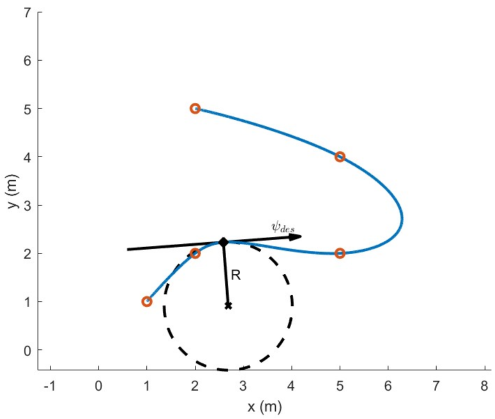

Figure 6: Path Reference Computation from Trajectory Spline

4. Simulation

This section presents a numerical simulation in MATLAB that demonstrates all parts of the previously presented algorithms working as part of the full system and allows initial study of the system performance. The bicycle model from Section 2.1 was used along with a tangent frame mechanization to simulate the vehicle states and maneuvers throughout e-stop operations. In all cases presented in this section, the vehicle was initialized at a nominal velocity and given waypoints that define the last known safe path for the e-stop to follow before an e-stop was triggered. Knowledge of the vehicle's lateral velocity state was generated using a linear Kalman filter.

4.1. Baseline Performance

In the nominal version of this simulation, the controller was given exact knowledge of the vehicle model parameters. Figure 7 shows this nominal setup operating on a set of waypoints that define a single lane change avoidance maneuver where the e-stop was triggered when the vehicle was traveling at 15 m/s.

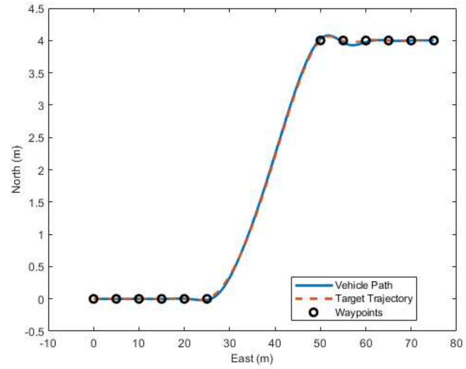

Figure 7: Single Lane Change E-Stop (15 m/s)

The path tracking error states for this maneuver are shown in Figure 8. The peak lateral error is approximately 5 cm, occurring during the lane change transition, and all error states converge back to zero as the vehicle settles into the new lane and comes to a stop.

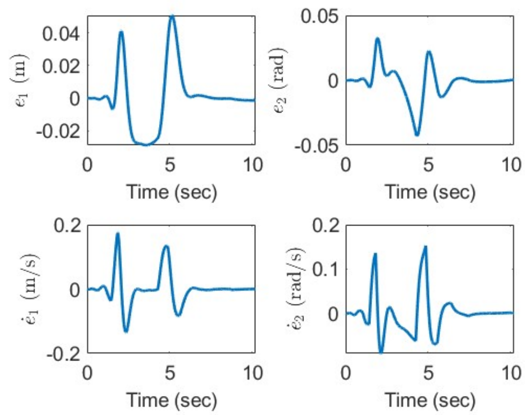

Figure 8: Path Tracking Error States for Single Lane Change E-Stop

4.2. Friction-Aware Velocity Planning

Although the baseline system minimizes dynamic requirements through the minimum jerk trajectory, a constant braking reference does not account for the lateral forces encountered during turns [8]. At higher speeds, the combined longitudinal and lateral tire force demands can exceed the available tire force, risking loss of control.

In vehicle dynamics, the forces available at each tire are bounded by a friction circle [10, 15]. The combined lateral (F_y) and longitudinal (F_x) force at a tire must satisfy:

$$\sqrt{F_x^2 + F_y^2} \leq \mu F_z \qquad (20)$$

where μ is the road friction coefficient and F_z is the tire's normal load. Reducing the peak of the combined acceleration vector therefore increases the safety margin inside the friction circle. Because tire parameters and loading are never known exactly, a larger gap between the operating point and the friction boundary translates directly into greater tolerance of modeling error. The point of greatest concern is where the lateral acceleration $a_y = v_x^2/R$ peaks along the trajectory under the nominal braking plan.

To exploit this relationship, the braking profile is split into two segments at the point of peak lateral demand, as illustrated in Figure 9. In the first segment the vehicle decelerates at a higher rate, arriving at the critical point with a lower speed and correspondingly lower lateral force. In the second segment a gentler deceleration brings the vehicle to rest by the end of the path. The transition speed is chosen so that the total acceleration magnitude is uniform across both segments ($\|a_1\| = \|a_2\|$). In the approach segment only longitudinal braking contributes, while through the turn the magnitude also includes the lateral component, $\|a_2\| = \sqrt{a_x^2 + a_y^2}$. This balances the tire force demands across the maneuver rather than concentrating them at the turn. For a straight approach such as a single lane change, $\|a_1\|$ reduces to the longitudinal braking acceleration alone. On curved roads, $\|a_1\|$ also includes the lateral acceleration due to the road curvature.

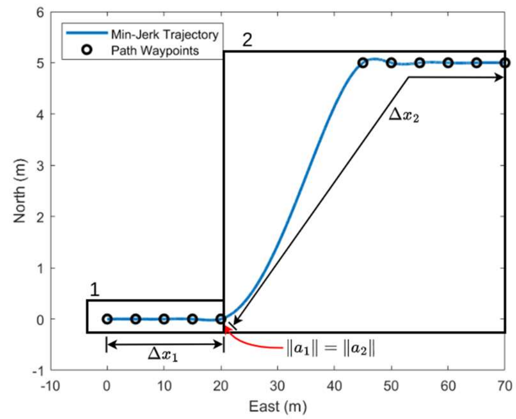

Figure 9: Acceleration Regions for Friction-Aware Velocity Planning

To demonstrate the need for this method, the simulation was repeated at an initial velocity of 20 m/s. At this higher speed, the lateral acceleration demands through the turn increase significantly due to the v_x^2/R relationship. Figure 10 shows the front tire forces for this case using the unmodified constant braking plan. The tire forces exceed the friction circle boundary during the turn, indicating that tire saturation would likely occur in practice. Figure 11 shows the same scenario with the friction-aware velocity plan applied. The vehicle arrives at the turn at a reduced speed, keeping the tire forces within the friction circle throughout the maneuver.

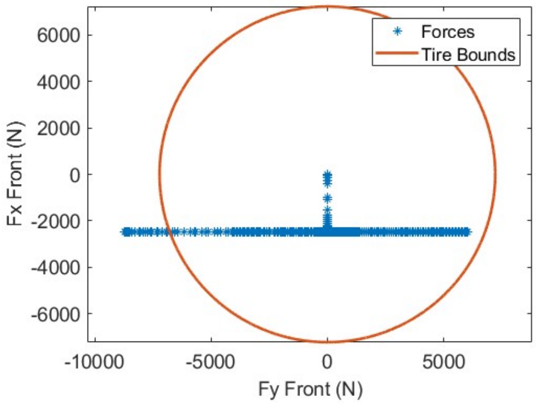

Figure 10: Front tire forces without friction-aware velocity planning (20 m/s). Forces exceed the friction circle during the turn.

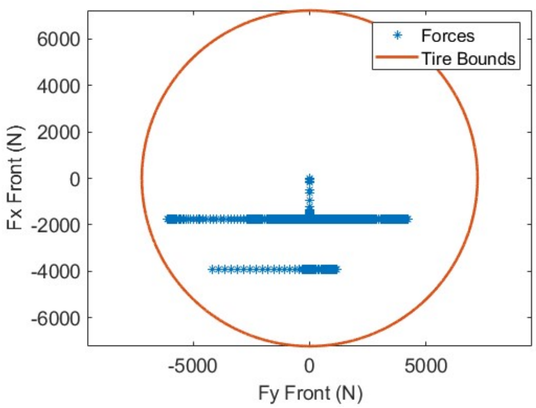

Figure 11: Front tire forces with friction-aware velocity planning (20 m/s). Forces remain within the friction circle.

4.3. Monte Carlo Robustness Analysis

All preceding results use the exact plant parameters inside the controller. In practice, however, an e-stop system must be robust enough to allow for model imperfections. During early development the vehicle may not be fully characterized, and the emergency itself may have been triggered by unexpected changes in vehicle behavior. Mass, inertia, and tire stiffness can all vary with loading, wear, and surface conditions. To quantify sensitivity, a 1000-trial Monte Carlo study was performed. Each trial drew its plant parameters from the Gaussian distributions listed in Table 3, with nominal values sourced from [16], whereas the controller retained the nominal values throughout. A brake efficiency factor scales the available longitudinal force in each trial to represent degraded surface grip. Simulated sensor noise was also added to the yaw and yaw rate measurements to verify robustness of the state estimator under realistic conditions. The standard deviations of this sensor noise were:

$$\sigma_\psi = 0.004 \text{ rad}$$

$$\sigma_{\dot{\psi}} = 0.000192 \text{ rad/s}$$

Table 3. Monte Carlo Randomized Parameters

Parameter	**Design**	Sim $\mathcal{N}(\mu, \sigma)$
a (m)	1.257	$\mathcal{N}(1.257,\ 0.2)$
b (m)	1.593	$\mathcal{N}(1.593,\ 0.2)$
m (kg)	1857	$\mathcal{N}(1857,\ 100)$
I_z (kg $\cdot$ m^2)	4292	$\mathcal{N}(4292,\ 200)$
C_{α_f} (N/rad)	120000	$\mathcal{N}(120\text{k},\ 12\text{k})$
C_{α_r} (N/rad)	184600	$\mathcal{N}(184.6\text{k},\ 18.5\text{k})$
Brake Eff.	1.0	0.85

The path tracking results across all 1000 runs are shown in Figure 12. Despite the parameter variation, the vehicle consistently follows the reference trajectory. Figure 13 shows the lateral error states for all runs. Worst-case lateral deviation across all trials reached roughly 10 cm.

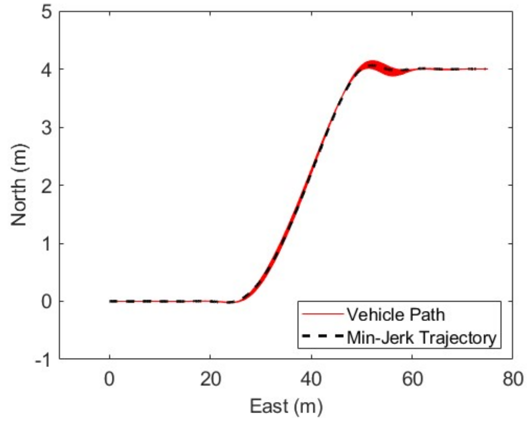

Figure 12: Monte Carlo Path Tracking Results (1000 runs)

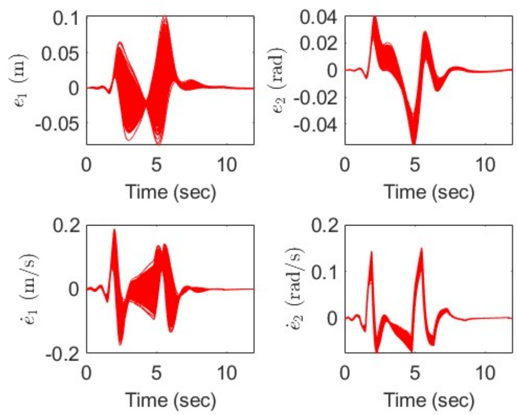

Figure 13: Monte Carlo Lateral Error States

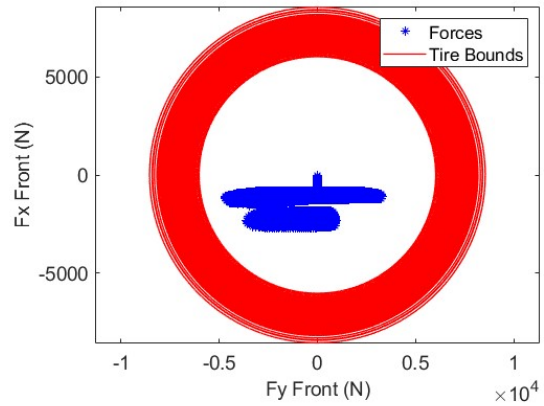

Figure 14: Monte Carlo Front Tire Forces (1000 runs)

Most critically, Figure 14 shows the front tire forces across all 1000 runs. Each run's friction circle was computed from its own randomized parameters, so the plot contains 1000 individual friction circle boundaries alongside the corresponding force trajectories. Across every trial and every time step, the resultant tire force remained inside its corresponding friction circle, verifying that the velocity planning strategy preserves adequate force margin under the tested range of parameter variation.

5. Experiment

The preceding simulation verified the system performance and enabled analysis of quantities that are not directly measurable during live testing, such as instantaneous tire forces and sensitivity to model parameter uncertainty. This section presents the experimental verification of the system operating in real time on the target embedded hardware.

5.1. Computing Hardware

The e-stop controller runs on a low-cost single board computer positioned as a gateway on the vehicle's CAN bus, between the primary autonomy stack and the drive-by-wire interface. Under normal conditions the gateway is transparent, forwarding all bus traffic unchanged. Upon activation, it intercepts outgoing commands and substitutes its own control outputs. Because the gateway operates independently, it retains full braking authority even if the upstream autonomy computer becomes unresponsive.

Several low-cost computing platforms were evaluated for the e-stop system, summarized in Table 4.

Table 4. Low-Cost Computing Platform Comparison

Board	Price	RAM	Processor
Teensy 4.1 [17]	$39.60	1024 KB	600 MHz
RPi Pico 2 [18]	$5.00	520 KB	150 MHz
RPi Zero 2 [19]	$15.00	512 MB	1 GHz
RPi 4 1GB [20]	$35.00	1 GB	1.8 GHz

The deciding factor in platform selection was working memory rather than processor clock speed, because the QP solver used for trajectory optimization requires a memory allocation that exceeds what microcontroller-class boards can provide. The Teensy 4.1 offers a 600 MHz processor but only 1024 KB of SRAM, which proved insufficient for the solver's workspace. The Pico 2, while less expensive, was further limited by slow floating-point operations. Ultimately the Pi Zero 2 represented the most economical board with adequate memory and processing capability.

All algorithms were compiled into a single C++ binary targeting the Pi Zero 2. The trajectory QP was auto-generated from its MATLAB prototype with MATLAB Coder, while the Kalman filter's matrix exponential was computed via a truncated power series, as no suitable linear algebra library was available on the target ARM platform. On this hardware the control loop averages 700 Hz, however, the serial link to the host computer constrains the effective update rate to 500 Hz. The QP solver executes once at trigger time and converges within roughly half a second.

5.2. Live Vehicle Testing

The system was tested on an autonomous 2017 Lincoln MKZ, shown in Figure 15, equipped with a DataSpeed drive-by-wire kit, GPS/INS for localization, and a standalone IMU for yaw rate measurements. The Raspberry Pi Zero 2 communicated with the main vehicle computer via a serial USB link. Testing was conducted on the skid pad at Auburn University's National Center for Asphalt Technology (NCAT) test track facility at an initial velocity of approximately 30 mph (13.4 m/s), with the e-stop commanding a 4-meter single lane change maneuver while bringing the vehicle to a stop.

Figure 15: DataSpeed Lincoln MKZ

Figure 16 shows the vehicle's path during one of these maneuvers alongside the generated minimum-jerk trajectory. The vehicle closely follows the reference path, with small deviations visible near the lane change transition.

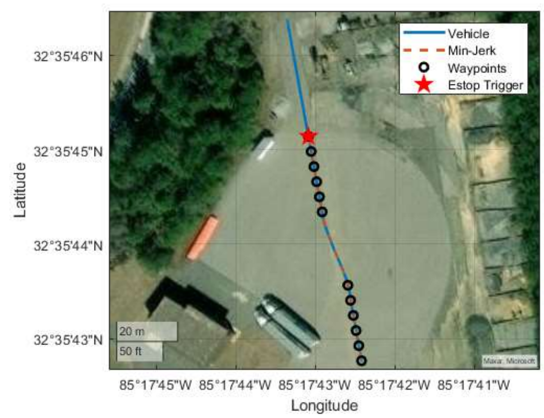

Figure 16: Experimental E-Stop Maneuver (30 mph)

Figure 17 shows the absolute distance between the vehicle position and its nearest trajectory point. Peak deviations remain below 15 cm and coincide with the steering transient at the lane change onset. Steering actuator bandwidth is the dominant contributor to this tracking offset.

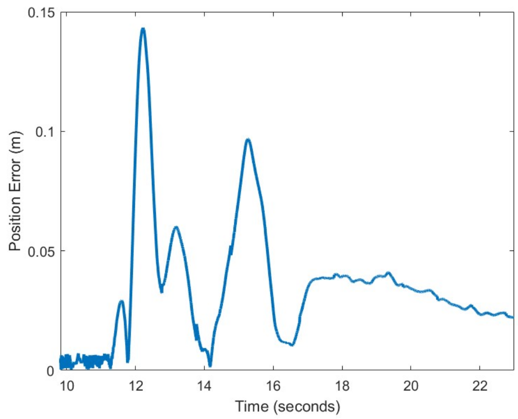

Figure 17: Experimental Position Tracking Error (30 mph)

The velocity response during the maneuver is shown in Figure 18. The velocity plot clearly shows the two-segment deceleration strategy: a heavier initial brake application reduces speed ahead of the lane change, followed by a gentler ramp to zero once lateral demands subside. An initial delay of roughly 0.5 s corresponds to the on-board QP solver. After that, control updates keep pace with the vehicle without measurable latency.

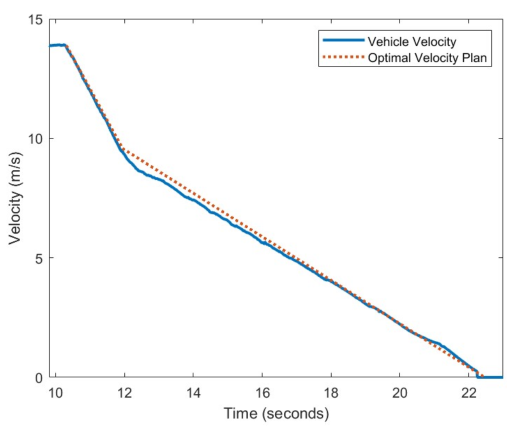

Figure 18: Experimental Velocity Response (30 mph)

6. Conclusions

This paper presented an intelligent emergency stop system for autonomous ground vehicles that combines minimum-jerk trajectory optimization, LQR path tracking control, and friction-aware velocity planning, all running on a low-cost embedded gateway.

In simulation, the optimized minimum-jerk paths exhibited substantially reduced peak lateral accelerations compared to standard cubic spline interpolation, directly increasing the available safety margin within the tire friction envelope. The two-phase braking strategy kept resultant tire forces inside the friction circle by redistributing deceleration effort relative to the point of greatest lateral demand. A Monte Carlo campaign of 1000 trials, each sampling vehicle parameters from distributions with standard deviations up to 10% of their nominal values, produced worst-case lateral deviations under 10 cm, indicating strong tolerance to parametric uncertainty.

Live vehicle trials demonstrated on a Lincoln MKZ at 30 mph confirmed real-time execution of the complete algorithm suite on a $15 Raspberry Pi Zero 2. Lateral deviations stayed within 15 cm throughout every run, well inside typical lane-marking tolerances, demonstrating that the low-cost hardware imposes no meaningful penalty on tracking accuracy. The CAN bus gateway architecture adds a layer of fault tolerance that is particularly relevant for fielded UGVs. The e-stop hardware is electronically and computationally independent, therefore it can bring the vehicle to a safe stop even after a total loss of the primary autonomy stack.

Planned future developments include adapting the LQR weighting matrices as a function of speed through gain scheduling, embedding dynamic feasibility constraints directly into the trajectory QP, and replacing the decoupled lateral/longitudinal architecture with a unified model predictive controller.

7. References

[1] F. Favarò, S. Eurich, and N. Nader, “Autonomous vehicles' disengagements: Trends, triggers, and regulatory limitations,” Accident Analysis & Prevention, vol. 110, pp. 136–148, 2018.

[2] H. Li, T. Zheng, F. Xia, L. Gao, Q. Ye, and Z. Guo, "Emergency collision avoidance strategy for autonomous vehicles based on steering and differential braking," Scientific Reports, vol. 12, p. 22647, 2022.

[3] S. Kwon, C. Jung, T. Choi, Y. Oh, and B. You, "Autonomous emergency stop system," in 2014 IEEE Intelligent Vehicles Symposium Proceedings, pp. 444–449, IEEE, 2014.

[4] H. Pan, M. Luo, J. Wang, T. Huang, and W. Sun, "A Safe Motion Planning and Reliable Control Framework for Autonomous Vehicles," IEEE Transactions on Intelligent Vehicles, vol. 9, no. 4, pp. 4780–4793, 2024.

[5] E. Lowe and L. Guvenc, "Autonomous Vehicle Emergency Obstacle Avoidance Maneuver Framework at Highway Speeds," Electronics, vol. 12, p. 4765, 2023.

[6] R. Krauss, "Combining Raspberry Pi and Arduino to form a low-cost, real-time autonomous vehicle platform," in 2016 American Control Conference (ACC), pp. 6628–6633, IEEE, 2016.

[7] J. R. Ziehn, Beyerer, Filsinger, Roschani, Ruf, Flad, Frey, Hohmann, Knoch, Lauber, Pistorius, and Kohlhaas, "General Fail-Safe Emergency Stopping for Highly-Automated Vehicles," in Tagung Automatisiertes Fahren 2019, 2019.

[8] K. Thompson, "Intelligent Emergency Stop System for Autonomous Ground Vehicles Using Minimum Jerk Trajectories and Path Tracking Linear Quadratic Regulator," Master's thesis, Auburn University, 2025.

[9] R. Rajamani, Vehicle Dynamics and Control. Mechanical Engineering Series, Boston, MA: Springer US, 2012.

[10] T. D. Gillespie, Fundamentals of Vehicle Dynamics. Society of Automotive Engineers, 1992.

[11] R. N. Jazar, Vehicle Dynamics: Theory and Applications. New York, NY: Springer, 2009.

[12] N. V. M. Veerapaneni, "Real-time Minimum Jerk Optimal Trajectory Synthesis and Tracking for Ground Vehicle Applications," Master's thesis, University of Texas at Arlington, 2017.

[13] D. Mellinger and V. Kumar, "Minimum snap trajectory generation and control for quadrotors," in 2011 IEEE International Conference on Robotics and Automation, pp. 2520–2525, IEEE, 2011.

[14] R. F. Stengel, Optimal Control and Estimation. Dover Publications Inc., New York, 1994.

[15] A. Bhoraskar and P. Sakthivel, "A review and a comparison of Dugoff and modified Dugoff formula with Magic formula," in 2017 International Conference on Nascent Technologies in Engineering (ICNTE), pp. 1–4, IEEE, 2017.

[16] R. Brothers, "Path Following and Obstacle Avoidance for Autonomous Ground Vehicles Using Nonlinear Model Predictive Control," Master's thesis, Auburn University, 2020.

[17] PJRC, "Teensy® 4.1 Development Board." https://www.pjrc.com/store/teensy41.html. Accessed: 2024-11-21.

[18] Raspberry Pi, Raspberry Pi Pico 2 Datasheet. Raspberry Pi, 2024.

[19] Raspberry Pi, "Raspberry Pi Zero 2 W." https://www.raspberrypi.com/products/raspberry-pi-zero-2-w/. Accessed: 2024-11-21.

[20] Raspberry Pi, "Raspberry Pi 4 Tech Specs." https://www.raspberrypi.com/products/raspberry-pi-4-model-b/specifications/. Accessed: 2024-11-21.

8. Contact Information

Kyle Thompson

Graduate Research Assistant

Auburn University

Department of Mechanical Engineering

Wiggins Hall

354 War Eagle Way

Auburn, AL 36849

kat0028@auburn.edu
256-603-2486

David M. Bevly, PhD
Bill and Lana McNair Distinguished Professor
Auburn University
Department of Mechanical Engineering
Wiggins Hall
354 War Eagle Way
Auburn, AL 36849
bevlydm@auburn.edu
(334) 844-3446